Noncollinear Antiferromagnets for Memory Applications and Beyond

BERNHARD PRUCKNER[1], NILS PETTER JORSTAD[1,2], WOLFGANG GOES[3],
SIEGFRIED SELBERHERR[2], VIKTOR SVERDLOV[2]
[1]Christian Doppler Laboratory for Nonvolatile Magnetoresistive
Memory and Logic, Vienna,
AUSTRIA

[2]Institute for Microelectronics, TU Wien,
Gußhausstraße 27–29/E360, 1040 Vienna,
AUSTRIA

[3]Silvaco Europe Ltd., Cambridge,
UNITED KINGDOM

Abstract - Noncollinear antiferromagnets (nc-AFMs) have gained attention for their potential use as spin-polarizing layer in novel magnetoresistive random access memory (MRAM) devices, due to the magnetic spin Hall effect (MSHE). Furthermore, strained nc-AFMs show a small but nonzero net-magnetization, that can be switched by spin-polarized current, making them suitable as magnetic memory layers as well. This work explores the switching dynamics of the nc-AFM Mn_3Sn. We demonstrate, that deterministic switching in an Pt/Mn_3Sn bilayer is achieved by controlling an applied charge current and external magnetic field. Furthermore, we explore possible mechanisms for fully electric mutual magnetization reversal in an Mn_3Sn/Mo/CoFeB trilayer. We identify spin-orbit precession (SOP) at the Mo/CoFeB interface as well as the MSHE in the bulk of Mn_3Sn as possible driving mechanisms. We demonstrate that through mutual switching in the trilayer-device, the polarization direction of MSHE-generated spin current can be electrically controlled.

Key-Words: - Spin-Orbit Torque (SOT), Magnetization Switching, Field-Free Switching, Kagome Plane, Noncollinear Antiferromagnets, Trilayer

Received: June 13, 2025. Revised: September 26, 2025. Accepted: December 29, 2025. Published: May 27, 2026.

1 Introduction

Magnetoresistive random access memory (MRAM) is a novel memory technology, that shows high endurance, high energy efficiency, and switching times in the sub-nanosecond regime, [1], with the potential to replace flash memory, DRAM, and cache memory, [2], [3], [4]. The state of the cell is stored through the relative orientation of the magnetization of a perpendicularly magnetized ferromagnetic (FM) free layer (FL) and a magnetically fixed reference layer (RL) within a perpendicular magnetic tunnel junction (pMTJ). Spin Orbit Torque (SOT) MRAM have been proven to provide an effective approach to manipulate the magnetization of an FL with sub-ns switching speeds, [5], [6], [7], [8], [9], [10], [11]. However, to achieve full perpendicular deterministic magnetization reversal, typically an additional external field is required, which is detrimental to the density of SOT-MRAM devices, limiting scalability. Noncollinear antiferromagnets (nc-AFM) have been studied for their potential use as spin-polarizing layer in SOT-MRAM devices, due to the Magnetic Spin Hall Effect (MSHE), [12], [13]. The generation of out-of-plane spin-polarized spin currents by the MSHE facilitates field-free switching, eliminating the need of external magnetic fields in SOT-MRAM devices, while maintaining switching performance comparable to conventional magnetic field-assisted devices, [14]. Furthermore, introducing epitaxial tensile strain to the nc-AFM breaks the crystal symmetry, leading to a small nonzero net-magnetization, which can be manipulated by SOTs impinging from an adjacent heavy metal (HM) layer, proving the potential use of the nc-AFM film as magnetic memory layer, [15], [16], [17], [18]. Fig. 1a illustrates the arrangement of the Mn and Sn atoms within the two-dimensional kagome plane of the nc-AFM Mn_3Sn. The three sub-magnetic moments $\mathbf{m}_A$, $\mathbf{m}_B$ and $\mathbf{m}_C$, indicated by red arrows, carried by the Mn atoms are arranged in a triangular shape. The triangle of a neighboring kagome layer is represented by light blue spheres and dark red arrows. The order parameter established to describe the chiral structure of nc-AFMs such as Mn_3Sn is the octupolmoment, [15], [17], which is described by eq. (1),

$$\mathbf{m}_{\mathrm{Oct}} = \frac{1}{3}\mathbf{M}_{\mathrm{xy}}\left[\mathbf{m}_{\mathrm{A}} + \mathbf{R}_{\mathrm{y}}\left(\frac{-2\pi}{3}\right)\mathbf{m}_{\mathrm{B}} + \mathbf{R}_{\mathrm{y}}\left(\frac{2\pi}{3}\right)\mathbf{m}_{\mathrm{C}}\right] \tag{1}$$

with $\mathbf{M}_{xy}$ being the mirror operator in the xy-plane and $\mathbf{R}_y$ being the rotation operator around the y-axis.

The nearest neighbor magnetic moments are coupled via antiferromagnetic exchange, and each magnetic moment exhibits an individual magnetic anisotropy along the easy axes designated as $\mathbf{e}_{k,A}$, $\mathbf{e}_{k,B}$ and $\mathbf{e}_{k,C}$. Fig. 1b depicts individual Mn atom anisotropy, intralayer and interlayer exchange as well as the DMI acting on the sub-moments, [19]. In an unstrained state, the mag-

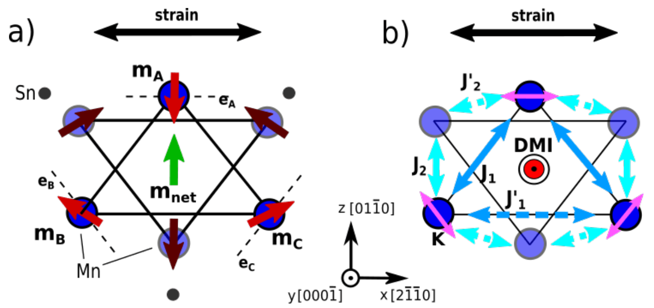

Fig. 1 | Structure of Mn_3Sn. *Source: created by the authors.* **a** Sketch of the magnetic structure of the nc-AFM Mn_3Sn. Mn (blue spheres) and Sn (dark grey spheres) atoms form a kagome lattice. The light blue spheres represent the Mn atoms of the neighboring kagome layer. Red arrows indicate the direction of the sub-magnetic moments $\mathbf{m}_A$, $\mathbf{m}_B$ and $\mathbf{m}_C$, which form a triangle within a kagome layer. The black dashed lines represent the individual Mn atom magnetic easy axes. The green arrow represents the net-magnetic moment $\mathbf{m}_{net}$, which emerges when tensile strain is applied to the crystal structure. **b** The kagome structure with indicated intralayer exchange (blue arrows), interlayer exchange (turquoise arrows), individual Mn anisotropy (pink arrows) and DMI (red out-of-plane arrow). Strain modulates exchange energy along strain-direction, indicated by the dashed blue and turquoise arrows.

netic sub-moments cancel out and the net-magnetization $\mathbf{m}_{net} = \mathbf{m}_A + \mathbf{m}_B + \mathbf{m}_C$ is zero. Applying tensile strain breaks the crystal symmetry and a small nonzero $\mathbf{m}_{net}$ emerges. The exchange interaction along strain-direction is modulated. For a static state $\mathbf{m}_{net}||\mathbf{m}_{Oct}$, [16].

In Section II. we describe the model utilized in our simulations, employing the Landau-Lifshitz-Gilbert (LLG) equation, [20], [21]. We outline our coupled spin and charge drift-diffusion model used to describe spin currents arising in the considered devices. In Section III. we investigate SOT-driven magnetization dynamics of the strained nc-AFM Mn_3Sn in a Pt/Mn_3Sn bilayer, where spin currents are generated by the SHE in the Pt layer.

An electrically controlled mutual magnetization reversal of individual magnetic domains in an Mn_3Sn and a CoFeB layer respectively, has been reported in Mn_3Sn/Mo/CoFeB trilayer structures, [22]. While a partially compensated spin current-driven switching of the CoFeB and Mn_3Sn layers has been attributed to a multi-domain structure, we provide a comprehensive single-domain model, that nonetheless exhibits electrically controlled mutual switching due to MSHE and spin current generation at the Mo/CoFeB interface arising from spin-orbit coupling (SOC). In Section IV. we investigate spin-polarizing mechanisms in a Mn_3Sn/Mo/CoFeB trilayer, focusing on the MSHE in the bulk of the Mn_3Sn as well as SOC interface effects such as spin-orbit precession (SOP) at the Mo/CoFeB interface. In Section V. we show results of our simulations of the trilayer structure, identifying possible mechanisms behind the field-free fully electrical mutual switching as well as the electric control of spin-polarization in the Mn_3Sn layer.

2 Modeling of Mn_3Sn

We employ a six-spin model to describe the magnetization dynamics of the nc-AFM Mn_3Sn. We consider the three sub-moments $\mathbf{m}_A$, $\mathbf{m}_B$ and $\mathbf{m}_C$ of two neighboring kagome planes, which allows to attribute not only for nearest neighbor intralayer interactions, but also interlayer effects across two neighboring kagome planes. In our six-spin model the magnetic energy of an unstrained chiral nc-AFM can be described by eq. (2), [16],

$$E = -K_0 \sum_{ia} (\mathbf{m}_{ia} \cdot \mathbf{e}_{k,a})^2 + \sum_{ia,jb} J_{ia,jb}\ \mathbf{m}_{ia} \cdot \mathbf{m}_{jb} + \sum_{ia,jb} D_{ia,jb}\, \mathbf{e_D} \cdot (\mathbf{m}_{ia} \times \mathbf{m}_{jb}), \tag{2}$$

where the suffixes i, j denote the unit cell, and a, b denote the sub-spins of the nc-AFM. K_0 is the anisotropy constant for the individual Mn atoms, $J_{ia,jb}$ is the exchange constant, $D_{ia,jb}$ is the DMI constant, $\mathbf{m}$ is the normalized sub-magnetization vector, $\mathbf{e_k}$ is the unit vector of the easy axes of the individual Mn atoms, $\mathbf{e_D}$ is the DMI unit vector. The first term describes the anisotropy, which acts to align the individual magnetic sub-moments along their respective easy axes. The second term describes the antiferromagnetic exchange between nearest neighbor magnetic moments, which acts to align two neighboring magnetic moments antiparallel to each other. We consider intralayer exchange, with constant J_1, between nearest neighbors within a kagome plane and intralayer exchange, with constant J_2, between nearest neighbors across two neighboring kagome planes. The third term describes the DMI acting between nearest neighbor magnetic moments, in a similar fashion as the exchange interaction. When introducing tensile epitaxial strain to the crystal, the exchange interaction in strain-direction is modulated (as depicted in Fig. 1b). The exchange energy contribution originating from the strained state can be described by a modulation of those exchange contributions along strain direction. The respective exchange constant are modulated as follows: $J_1' = (1-\delta)J_1$ and $J_2' = (1-\delta)J_2$, with δ being an energy modulation factor, corresponding to the tensile strain strength. As values of the constants we use, [16]: $J_1 = 23.15$ meV, $J_2 = 17.53$ meV, $D = 0.833$ meV, $K_0 = 0.196$ meV. The explicit expression for the anisotropy, exchange and DMI contributions to the total energy respectively are presented in eq. (3). For simplicity we consider a three-spin model, only taking into account the three subspins in the top kagome layer, as depicted in Fig. 1.

$$E_K = -K_0 \left[(\mathbf{m}_A \cdot \mathbf{e}_A)^2 + (\mathbf{m}_B \cdot \mathbf{e}_B)^2 + (\mathbf{m}_C \cdot \mathbf{e}_C)^2 \right] \tag{3a}$$

$$E_J = J_1 \left(\mathbf{m}_A \cdot \mathbf{m}_B + \mathbf{m}_C \cdot \mathbf{m}_A \right) + J_1' \left(\mathbf{m}_B \cdot \mathbf{m}_C \right) \tag{3b}$$

$$E_D = D \left(\mathbf{m}_A \times \mathbf{m}_B + \mathbf{m}_B \times \mathbf{m}_C + \mathbf{m}_C \times \mathbf{m}_A \right) \tag{3c}$$

The exchange energy contribution between the sub-spins $\mathbf{m}_A$ and $\mathbf{m}_B$ is modulated, due to the crystal strain, as depicted in Fig. 1b. To acquire the six-spin model, the energy is complemented with intralayer exchange contributions, depicted in Fig. 1b as turquoise arrows. An unstrained nc-AFM crystal has a sixfold energy degeneracy, exhibiting six equal minimal energy states. When strain is applied the energy landscape shifts towards a twofold energy degeneracy, exhibiting two clearly distinct energy minima and maxima. Fig. 2a shows the energy profile of a Mn_3Sn unit cell for various δ. With increasing strain, the sixfold energy profile shifts towards a twofold energy profile, with two distinct energy maxima and minima. By applying an external magnetic field $\mathbf{H}_{\text{ext}}$ to a strained nc-AFM, the twofold energy peaks are shifted, according to the orientation of $\mathbf{m}_{\text{net}}$ with respect to the external field. The contribution of the external field to the total energy can be described by eq. (4),

$$E = -\mu_0 M_S\, \mathbf{H}_{\text{ext}} \cdot \mathbf{m}_{\text{net}} \tag{4}$$

where μ_0 is the vacuum permeability and $M_S = 3 * \mu_B$, [16], with μ_B being the Bohr magneton. Fig. 2b shows the energy of a strained Mn_3Sn depending on the angle θ_{Oct} between the octupolmoment $\mathbf{m}_{\text{Oct}}||\mathbf{m}_{\text{net}}$ and the z-axis for various external field $\mathbf{H}_{\text{ext}}$ strengths, applied along x-direction. The energy peak, that corresponds to the $\mathbf{m}_{\text{Oct}}$ direction parallel to $\mathbf{H}_{\text{ext}}$ is lowered, whereas the energy peak of antiparallel orientation is increased. The resulting shifted energy landscape with two energy peaks of different size facilitates the deterministic switching of $\mathbf{m}_{\text{net}}$. To model the current-induced dynamics of each Mn magnetic moment $\mathbf{m}_i$, we utilize eq. (5), which is the Landau-Lifshitz-Gilbert (LLG) equation with an additional torque term.

$$\frac{\partial \mathbf{m}_i}{\partial t} = -\gamma_0 \mathbf{m}_i \times \mathbf{H}_{\text{eff},i} + \alpha \mathbf{m}_i \times \frac{\partial \mathbf{m}_i}{\partial t} + \frac{1}{M_S}\mathbf{T}_{S,i} \tag{5}$$

The first and second term of the LLG equation describe the precession and damping of the normalized Mn magnetic moment $\mathbf{m_i}$ towards an effective field $\mathbf{H}_{\text{eff,i}}$ respectively. M_S is the single Mn atom magnetization. The third term describes the spin torques $\mathbf{T}_{\mathbf{S,i}}$ acting on the magnetic moments $\mathbf{m_i}$. $\gamma_0 = -\gamma\mu_0$ is the rescaled gyromagnetic ratio, and α is the dimensionless Gilbert damping constant. We obtain $\mathbf{H}_{\text{eff},\mathbf{i}} = -\left(1/\mu_0 M_S\right)\left(\partial E_i/\partial \mathbf{m}_i\right)$ by taking the derivative of the magnetic energy of the sub-magnetic moment i described by eq. (2) and eq. (4). The spin torque acting on the magnetic sub-moment is described by eq. (6). It is obtained from considering the spin angular momentum transferred to the magnetization, [21], [23]:

$$\mathbf{T}_{S,i} = \frac{\mathbf{m}_i \times \mathbf{S}}{\lambda_J^2} + \frac{\mathbf{m}_i \times (\mathbf{m}_i \times \mathbf{S})}{\lambda_\varphi^2} \tag{6}$$

D_e is the electron diffusion coefficient , λ_J, and λ_ϕ are the exchange, and dephasing lengths, respectively, and $\mathbf{S}$ is the nonequilibrium spin accumulation in units of A/m.

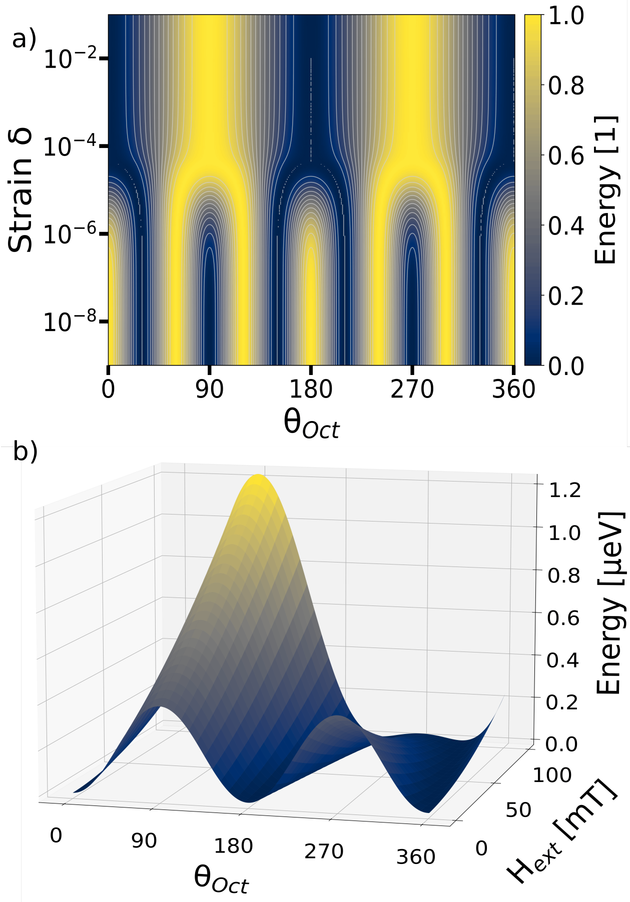

Fig. 2 | Energy landscape of Mn_3Sn. *Source: created by the authors.* **a** Normalized energy of a Mn_3Sn unit cell for various strengths of tensile strain, corresponding to the δ parameter. With increasing tensile strain in the crystal, the energy landscape shifts from a sixfold towards a twofold energy degeneracy, corresponding to two distinct stable magnetic configurations. **b** The twofold energy of a strained Mn_3Sn under an applied external magnetic field $\mathbf{H}_{\text{ext}}$. As the external field is increased, each of the two initially equal energy barriers is heightened or decreased, depending on the orientation of $\mathbf{m}_{\text{net}}$ of the corresponding state in respect to $\mathbf{H}_{\text{ext}}$.

3 Magnetization Switching of Mn_3Sn

Fig. 3 shows the bilayer SOT-device consisting of Mn_3Sn layer on top of a heavy metal Pt write layer. A charge current J_C is applied to the Pt layer in the x-direction. In the presented bilayer SOT-device, a spin current is generated in the HM layer according to eq. (7), mainly due to the Spin Hall effect (SHE), which flows perpendicularly to the applied charge current:

$$\overline{\mathbf{J}_{\mathbf{S}}}_{,\text{SHE}} = -\theta_{\text{SHE}}\hat{\epsilon}\,\mathbf{J}_{\mathbf{C}} \tag{7}$$

θ_{SHE} is the spin Hall angle and describes the charge-to-spin conversion by the SHE, and $\hat{\epsilon}$ is the $3 \times 3 \times 3$ Levi-Civita tensor. The spin Hall angle of Pt is $\theta_{\text{SHE|Pt}} = 0.19$. $\overline{\mathbf{J}_{\mathbf{S}}}$ describes the spin-current as 3×3 tensor. Spin current polarized along the y-direction impinges into the

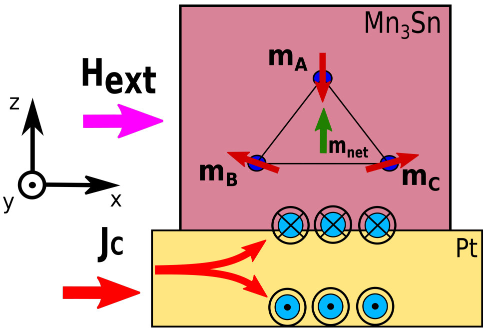

Fig. 3 | Pt/Mn_3Sn bilayer. *Source: created by the authors.* SOTs generated in the Pt layer by the spin Hall effect. An applied charge current $\mathbf{J}_C$ along x-direction generates spin current polarized along y-direction, impinging into the Mn_3Sn layer. There it drives magnetization dynamics of the Mn_3Sn. An applied external field $\mathbf{H}_{ext}$ shifts the twofold energy landscape of Mn_3Sn (as depicted in Fig. 2) and facilitates deterministic magnetization switching of $\mathbf{m}_{net}$.

Mn_3Sn layer. At the Pt/Mn_3Sn continuous boundary conditions for the spin current are applied. The spin current leads to a torque acting on the individual Mn magnetic moments $\mathbf{m}_i$. A spin current with a polarization direction normal to the kagome plane, drives switching of the Mn magnetic moments, and therefore switching of $\mathbf{m}_{net}$. Figs. 4a and b show simulation results for $\mathbf{m}_{net}/M_S$ of the Mn_3Sn layer under the influence of SOTs generated by applied current densities $J_c = 3.0 \times 10^{11}$ A/m^2, 6.5×10^{11} A/m^2 and 8.0×10^{11} A/m^2 without and with an applied external field $\mathbf{H}_{ext}$, respectively. Fig. 4c and Fig. 4d show the according energies for the applied current densities and the static energy of the system. A minimal current density is necessary to overcome the energy barrier of the system. This is why when a charge current of $J_c = 3.0 \times 10^{11}$ A/m^2 is applied, the generated SOTs cannot overcome the barrier, and no magnetization dynamics can be observed. Once a sufficiently strong current of $J_c = 6.5 \times 10^{11}$ A/m^2 is applied, the SOTs can overcome the energy barrier and drive ultra-fast oscillations of $\mathbf{m}_{net}$ in the sub-ns regime. Further increase in current density leads to faster oscillation. With an external field of $\mathbf{H}_{ext} = 0.1$ T applied, the energy landscape of the system is changed. The energy maximum corresponding to the orientation $\mathbf{H}_{ext}||\mathbf{m}_{net}$ is decreased, whereas the maximum corresponding to $\mathbf{H}_{ext}|| - \mathbf{m}_{net}$ is increased. Depending on the current strength, different behaviors of $\mathbf{m}_{net}$ can be observed: no dynamics, deterministic switching, and ultra-fast oscillations. When the energy barrier cannot be overcome with a current of $J_c = 3.0 \times 10^{11}$ A/m^2, no switching dynamics of $\mathbf{m}_{net}$ is observed. The applied current of $J_c = 6.5 \times 10^{11}$ A/m^2 is strong enough to overcome the first barrier, but not the second one. Thus the nc-AFM will exhibit deterministic switching of $\mathbf{m}_{net}$. A current of $J_c = 8.0 \times 10^{11}$ A/m^2 is strong enough to overcome both barriers and ultra-fast oscillations of $\mathbf{m}_{net}$ occur.

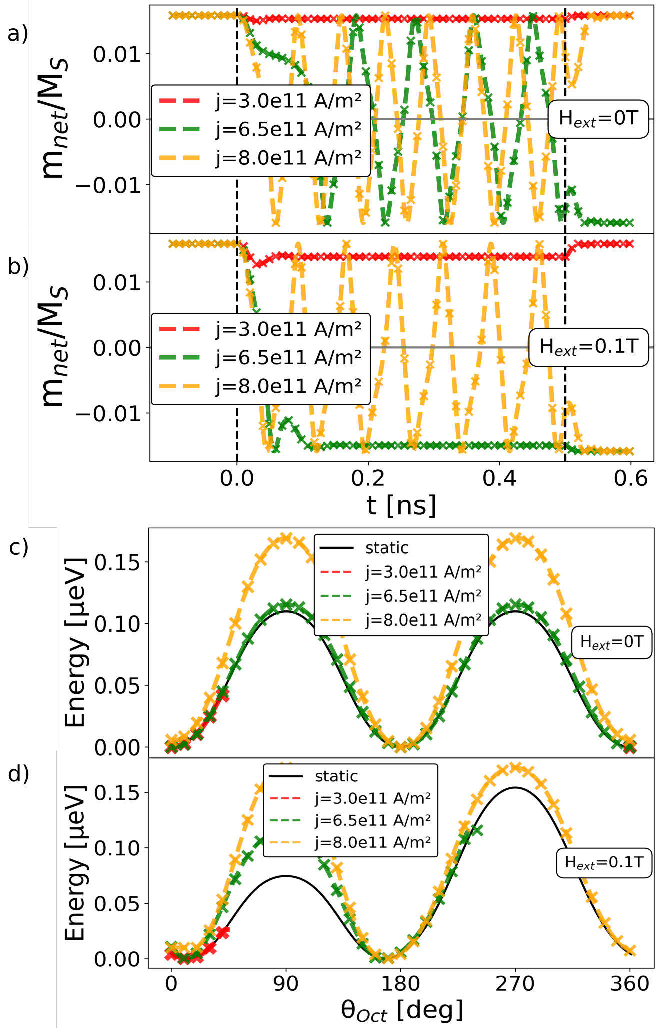

Fig. 4 | Nc-AFM switching in a Pt/Mn_3Sn bilayer. *Source: created by the authors.* **a-b** The net-magnetization $\mathbf{m}_{net}$ of Mn_3Sn in the bilayer structure from Fig. 3, for various current densities applied to the Pt layer, without **(a)** and with **(b)** an external magnetic field $\mathbf{H}_{ext}$ of 0.1T. **c-d** The static energy (black line) of a Mn_3Sn unit cell without **(c)** and with **(d)** $\mathbf{H}_{ext}$ respectively, as well as the corresponding energies of the system with a charge current applied to the Pt layer. Once the applied current densities, and thus the SHE-generated spin-currents impinging from the Pt-layer, are strong enough, the energy barriers can be overcome, which leads to SOT-induced oscillations of $\mathbf{m}_{net}$. Applying an external field $\mathbf{H}_{ext}$, leads to a shift of the energy peaks. In a shifted energy landscape, the first peak can be overcome, but not the second one, leading to deterministic switching of $\mathbf{m}_{net}$.

4 Spin Currents in an Mn_3Sn/Mo/CoFeB Trilayer

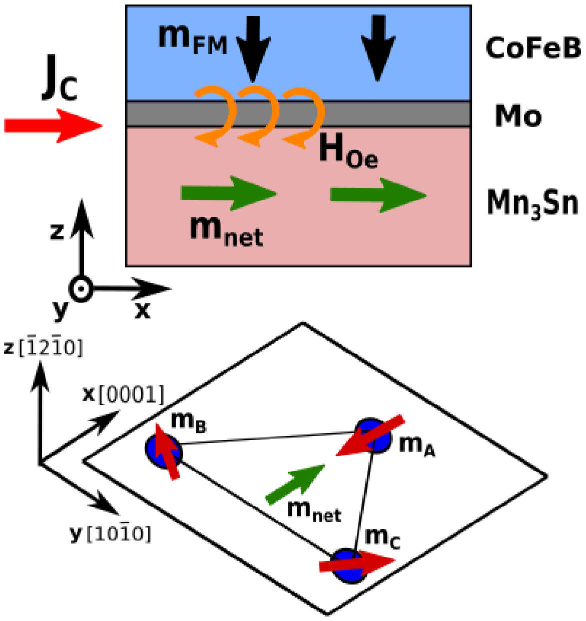

Fig. 5 | Mn_3Sn/Mo/CoFeB trilayer. *Source: created by the authors.* **a** Sketch of the trilayer structure, with the CoFeB magnetization $\mathbf{m}_{\text{FM}}$ (black arrows) and the Mn_3Sn net-magnetization $\mathbf{m}_{\text{net}}$ (green arrows) at initial position along -z and +x respectively. A charge current J_C along x is applied to the whole trilayer structure. The induced Oersted field $\mathbf{H}_{\text{Oe}}$ is depicted as orange arrows. **b** Orientation of the kagome plane within the trilayer structure. The kagome plane lies in the xy-plane.

In the following we investigate current polarization and mutual magnetization switching in a Mn_3Sn(9nm)/Mo(1nm)/CoFeB(5nm) trilayer structure as depicted in Fig. 5. The kagome plane of the Mn_3Sn layer lies in the xy-plane of the device. The black and green arrows depict the magnetic moment $\mathbf{m}_{\text{FM}}$ in the CoFeB layer and $\mathbf{m}_{\text{net}}$ in the Mn_3Sn layer respectively. The red arrow represents the charge current along x-direction, that is applied to the whole trilayer structure. The two binary states of the strained nc-AFM are along the positive and negative x-direction. The CoFeB layer exhibits a perpendicular anisotropy, with the easy axis along z-direction.

We identify two main mechanisms of spin-polarization in the trilayer: MSHE in the bulk of the Mn_3Sn layer and current polarization in the CoFeB layer, by transfer of angular momentum, due to subsequent spin-orbit precession (SOP) at the Mo/CoFeB interface.

In the bulk of the Mn_3Sn layer charge current is spin-polarized by the MSHE. The spin current generation can be described by eq. (8), [14]

$$\overline{\mathbf{J}_{\mathbf{S}}}_{,\text{MSHE}} = -\hat{\theta}_{\text{SCA}}\mathbf{J}_{\mathbf{C}}, \tag{8}$$

where $\hat{\theta}_{SCA} = \hat{\sigma}_{\mathbf{SH}}\rho$ is the $3\times3\times3$ spin-charge angle (SCA) tensor, that describes the charge-to-spin conversion, [24]. The SCA tensor is a generalization of the scalar spin Hall angle, used to describe the charge-to-spin conversion by the conventional SHE. $\hat{\sigma}_{\mathbf{SH}}$ is the $3\times3\times3$ spin Hall conductivity tensor (SHCT) and ρ is the electric resistivity. The configuration of the sub-spins of Mn_3Sn in the trilayer corresponds to the AFM2 state, [14]. The SHCT-component for AFM2 with a charge current applied along x-direction is described by eq. (9), which reads:

$$\sigma_{SH}^{S_x} = \begin{bmatrix} 0 & 0 & 0 \\ 0 & \sigma_{yy}^{x} & 0 \\ 0 & 0 & -\sigma_{zz}^{x} \end{bmatrix}. \tag{9}$$

The component σ_{zz}^{x} generates z-polarized spin current in z-direction when a charge current in x-direction is applied. This additional spin current component has been shown to facilitate field-free perpendicular magnetization switching in SOT-MRAM devices, incorporating Mn_3Sn as write line, instead of a conventional HM layer, [14]. The relevant $\hat{\theta}_{SCA}$ components for Mn_3Sn are $\theta_{SCA|Mn3Sn}^{y} = 0.221$ for generation of y-polarized spin current, and $\theta_{SCA|Mn3Sn}^{z} = 0.0673$ for generation of z-polarized spin current.

The spin-dependent current transport across the CoFeB/Mo interface is modeled by considering a strong Rashba spin-orbit interaction, which results in SOP-generated z-polarized spin current components impinging on the Mn_3Sn layer. The interface is described with a three-dimensional spin-dependent delta-function potential barrier at the interface. The Hamiltonian of the system is given by eq. (10):

$$\hat{H} = -\frac{\hbar^2}{2m_e}\nabla^2 + \delta(z)\left(V_0\hat{1} + J_{\text{ex}}\hat{\sigma}\cdot\mathbf{b}\right), \tag{10}$$

where $\hbar$, m_e, and ∇ are the reduced Planck's constant, electron mass, and Nabla operator, respectively. The hat (ˆ) denotes here a 2×2 matrix in spin-space, $\delta(z)$ is the Dirac delta function, and $\hat{\sigma}$ is the vector of the Pauli matrices. The vector $\mathbf{b}$ is the direction of the effective magnetic field at the interface that the electrons experience. The spin-independent potential energy is $V_0 = \hbar^2 k_F u_0/m_e$, while $J_{\text{ex}} = \hbar^2 k_F u_{ex}/m_e$ is the effective interfacial exchange energy, where u_0 and u_{ex} are the dimensionless magnitudes of each potential and k_F is the Fermi wave number. The differences between the two sides of the interface are captured by the nonequilibrium distribution functions and momentum-relaxation times at either side. For an interfacial exchange and Rashba spin-orbit interaction, one obtains $\mathbf{b}(\mathbf{k}) = (u_m\mathbf{m} + u_R\hat{\mathbf{k}}\times\hat{\mathbf{z}})/u_{\text{ex}}$ with $u_{\text{ex}} = \|u_m\mathbf{m} + u_R\hat{\mathbf{k}}\times\hat{\mathbf{z}}\|$, where u_m and u_R are the dimensionless magnitudes of both interactions, respectively, and $\mathbf{k}$ is the wave vector of the spins impinging the interface.

Spin-dependent reflection and transmission scattering matrices can then be obtained by considering specular scattering and plane-wave solutions of the time-independent Schrödinger equation with a spin quantization axis along $\mathbf{b}$, [25]. The expressions for the charge and spin current densities are then obtained from expanding the scattering matrices in terms of spin-projection matrices and

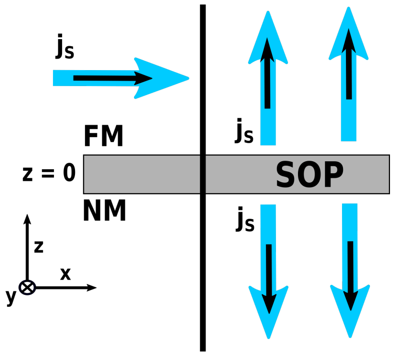

Fig. 6 | Spin-orbit precession (SOP) at a FM/NM interface. *Source: created by the authors.* A schematic illustration of the SOP mechanism at a FM/NM interface. Blue arrows represent the flow direction of the spin current, black arrows represent the polarization direction of the spin current. An in-plane charge current along x-direction generates an spin current in x-direction, with polarization direction according to the direction of $\mathbf{m}_{\mathrm{FM}}$ of the FM layer. SOP acting at the interface generates $-z$-polarized spin current flowing in $-z$-direction in the NM layer, given x-polarized spin current flowing in x-direction is present in the FM layer, [25].

averaging the scattered distribution functions over the momentum, [26]. For an electrical field E_x along the x-axis, the resulting out-of-plane spin current densities, with the spin polarization normal to the magnetization $\mathbf{m}$, at the interface are described by eq. (11), which read, [25]

$$\mathbf{J_{zs}}(0^+) = -\overline{G}_m \mathbf{V}_\mathbf{s}^{\mathrm{F}} + \overline{\Gamma}_m \mathbf{V}_\mathbf{s}^{\mathrm{N}} + P\overline{\sigma}_{ss}^{\mathrm{SOP}} \mathbf{m} E_x, \quad (11a)$$

$$\mathbf{J_{zs}}(0^-) = +\overline{G}_m \mathbf{V}_\mathbf{s}^{\mathrm{N}} - \overline{\Gamma}_m \mathbf{V}_\mathbf{s}^{\mathrm{F}} + P\overline{\gamma}_{ss}^{\mathrm{SOP}} \mathbf{m} E_x, \quad (11b)$$

where 0^+ and 0^- denote the CoFeB and Mo side of the interface respectively. $\overline{G}_m$ and $\overline{\Gamma}_m$ are interface mixing conductances and transmittances, obtained from the momentum averaging, [25]. The interface conductivities $\overline{\sigma}_{ss}^{\mathrm{SOP}}$, $\overline{\gamma}_{ss}^{\mathrm{SOP}}$ describe the current contributions from SOP. To model spin current generation at the Mo/CoFeB interface in the Mn_3Sn/Mo/CoFeB trilayer structure, we consider an in-plane current applied along x-direction (see Fig. 5). The generation of z-polarized spin current, necessary for switching of the nc-AFM is depicted in Fig. 6. To generate z-polarized spin current flowing in z-direction, x-polarized spin current flowing in x-direction needs to be present in the CoFeB layer, requiring $\mathbf{m}_{\mathrm{FM}}$ of the CoFeB layer to also exhibit a non-zero x-component, which is in fact the case, as shown in the following section. The spin current density in the layers flowing in z-direction are modeled in eq. (12) using drift-diffusion equations, [23], [27]:

$$\mathbf{J_{S,z}}(z) = -\sigma \frac{\partial \mathbf{V_S}(z)}{\partial z} + P\sigma \mathbf{m} \frac{\partial V_C(z)}{\partial z} \quad (12)$$

V_C is the electrical potential, $\mathbf{V_S} = (e/\mu_B)(D_e/\sigma)\mathbf{S}$ is the spin accumulation in units of V, σ is the electrical conductivity, and P is the spin polarization of the current. It is assumed that the spin instantly adapts to changes in magnetization direction, as its dynamics is faster by three orders of magnitude, [28]. For a steady state, the continuity equations eq. (13) read, [23], [27]

$$\frac{\partial \mathbf{J_{S,z}}(z)}{\partial z} = -\sigma \frac{\mathbf{V_S}(z)}{\lambda_{sf}^2} - \sigma \frac{\mathbf{V_S}(z) \times \mathbf{m}}{\lambda_J^2} - \sigma \frac{\mathbf{m} \times (\mathbf{V_S}(z) \times \mathbf{m})}{\lambda_\phi^2}, \quad (13)$$

where λ_{sf} is the spin-flip length. In the nc-AFM the contribution of magnetization is not considered , since $\mathbf{m}_{\mathrm{net}}$ is negligibly small. At the interface, Eqs (11) are used as boundary conditions for the drift-diffusion equations. The interface parameters u_m and u_R are treated as fitting parameters. We tune our model to experimentally reported values for a Mo/CoFeB bilayer with a Mo-thickness of 1nm, [29]. The nonequilibrium spin accumulation and torques are obtained by solving eqs. (13) with (12).

5 Mutual Switching in an Mn_3Sn/Mo/CoFeB Trilayer

By applying a charge current J_C to the trilayer structure presented in section IV., we are able to perform a fully electric controlled switching of both, the magnetization $\mathbf{m}_{\mathrm{FM}}$ of the CoFeB layer and the net-magnetic moment $\mathbf{m}_{\mathrm{net}}$ of the Mn_3Sn layer. Fig. 7a shows $\mathbf{m}_{\mathrm{FM}}$ and Fig. 7b shows$\mathbf{m}_{\mathrm{net}}$. At $t = 0$ns a charge current $J_{C1} = 8$mA is applied to the trilayer structure along x-direction, at $t = 1.0$ns a charge of $J_{C2} = 12$ mA is applied along x-direction and at $t = 1.2$ ns charge current $J_{C1} = 8$ mA is applied again. At $t = 2.1$ns the stronger charge current of $J_{C2} = 12$ mA is applied along x-direction again and at $t = 2.3$ns the weaker charge current $J_{C1} = 8$ mA is applied again. The charge current densities in the layers are calculated according to the parallel circuit model and the electrical conductivities of the materials, [22], with the electric conductivities $\sigma_{\mathrm{CoFeB}} = 4.0 \times 10^6$ S/m, $\sigma_{\mathrm{Mo}} = 2.0 \times 10^7$ S/m and $\sigma_{\mathrm{Mn3Sn}} = 2.0 \times 10^7$S/m of CoFeB, Mo and Mn_3Sn respectively, [12], [30]. An Oersted field is generated by the charge current in the Mo layer according to Ampere's law $\mathbf{H}_{\mathrm{Oe}} = \mathbf{J_C}\, d/2$, with layer thickness d, [22]. The Oersted field produced by the current flowing through the Mo layer acts similar to the externally applied field applied to the bilayer structure discussed in sections II. and III.. $\mathbf{H}_{\mathrm{Oe}}$ shifts the energy maxima of the Mn_3Sn, facilitating deterministic switching of $\mathbf{m}_{\mathrm{net}}$ in the trilayer structure, without the need of an additionally applied external magnetic field.

When J_{C1} is applied to the structure at $t = 0$ns, the charge current leads to the generation of y- and z-polarized spin current in z-direction by the MSHE in the Mn_3Sn. The spin current impinges into the CoFeB layer and leads to torques acting on $\mathbf{m}_{\mathrm{FM}}$, driving magnetization reversal. $\mathbf{m}_{\mathrm{FM}}$ is deterministically reversed, due to z-polarized spin current generated by the MSHE in the Mn_3Sn layer. At the same time spin current generated at the Mo/CoFeB

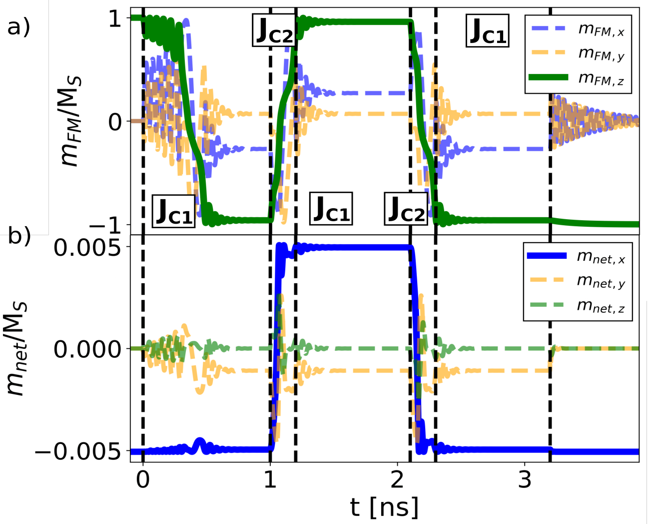

Fig. 7 | Mutual Switching of Mn_3Sn and CoFeB. *Source: created by the authors.* **a** The normalized magnetic moment $\mathbf{m}_{\text{FM}}/M_S$ of the CoFeB layer in the trilayer structure displayed in Fig. 5. **b** The net-magnetic moment $\mathbf{m}_{\text{net}}/M_S$ of the Mn_3Sn layer in the trilayer structure displayed in Fig. 5.
At t = 0ns a charge current of J_{C1} = 8mA is applied. At t = 1 ns a charge current of J_{C2} = 12mA. At t = 1.2 ns a charge current of J_{C1} = 8 mA is applied again. At t = 2.1 ns a charge current of J_{C2} = 12mA and at t = 2.3 ns a charge current of J_{C1} = 8 mA is applied again. At $t < 0$ns and $t > 3.2$ns no charge current is applied.
Due to spin currents generated by SHE in the Mn_3Sn and SOP at the CoFeB/Mo interface an electrically controlled windmill-type switching can be achieved.

interface impinges into the Mn_3Sn layer. Only spin current components polarized normal to the kagome plane drive switching of $\mathbf{m}_{\text{net}}$. As the kagome plane of Mn_3Sn in the trilayer structure lies within the xy-plane, only the spin current component polarized in z-direction impinging into the nc-AFM layer can drive magnetization reversal. Spin current during J_{C1} is too weak to drive a reversal of $\mathbf{m}_{\text{net}}$.

When the larger current J_{C2} is applied at t = 1.0ns, the z-polarized spin current produced at the Mo/CoFeB interface is sufficiently strong to drive the ultrafast magnetization dynamics of $\mathbf{m}_{\text{net}}$. The orientation of $\mathbf{m}_{\text{net}}$ is reversed. The Oersted field $\mathbf{H}_{\text{Oe}}$, generated by the charge current flowing through the Mo layer, shifts the twofold energy landscape of the Mn_3Sn. Therefore ultrafast sub-ns deterministic switching of $\mathbf{m}_{\text{net}}$ can be observed while applying J_{C2}.

Due to the reversed orientation of $\mathbf{m}_{\text{net}}$ and the strong applied current, the now oppositely polarized MSHE-generated spin current switches $\mathbf{m}_{\text{FM}}$ of the CoFeB layer back immediately to its original orientation. Now the cycle continues further. During the second J_{C2} pulse, the z-polarized spin current generated at the Mo/CoFeB interface impinges into the Mn_3Sn layer and switches $\mathbf{m}_{\text{net}}$ back to its original orientation. Due to the now again changed polarity of the MSHE-generated z-polarized spin current and the strong applied charge current $\mathbf{m}_{\text{FM}}$ follows with orientation reversal immediately. With this scheme, we can produce a windmill-like mutual switching, purely controlled by strength of the applied charge current in $+x$-direction.

We show that considering MSHE-driven spin-polarization in the bulk of Mn_3Sn and SOP at the Mo/CoFeB interface in an Mn_3Sn/Mo/CoFeB trilayer, provides an explanation for fully electric field-free switching. The out-of-plane z-polarized spin current component generated by the MSHE impinges into the CoFeB layer and drives field-free magnetization reversal of the magnetization in CoFeB. On the other hand, when increasing the current, the z-polarized spin current generated at the Mo/CoFeB interface impinging into the Mn_3Sn layer, becomes strong enough, to drive ultrafast dynamics of the net-magnetization in the nc-AFM. The intrinsically generated Oersted field shifts the energy profile of the Mn_3Sn and facilitates deterministic switching of the nc-AFM. The cycle can be continued, leading to windmill-like mutual switching, controlled by the strength of an applied charge current along x-direction. This is in contrast to, [22] where only the orientation of some weak domains in both CoFeB and Mn_3Sn was inverted. The presented scheme also provides an efficient way to control $\mathbf{m}_{\text{net}}$ in an nc-AFM layer, and therefore controlling the polarization of MSHE-generated spin current.

6 Conclusion

We present a micromagnetic model of the nc-AFM Mn_3Sn and show that ultrafast SOT driven magnetization dynamics are strongly dependent on tensile strain in the nc-AFM crystal, as well as an applied magnetic field, which shifts the energy landscape, facilitating deterministic magnetization reversal in a Pt/Mn_3Sn bilayer. Furthermore, we explore possible mechanisms for fully electric mutual magnetization reversal in a Mn_3Sn/Mo/CoFeB trilayer. Applying an in-plane charge current leads to spin current generation by the MSHE in the Mn_3Sn and by SOP interface effects at the Mo/CoFeB interface. Depending on the strength of the applied charge current and the orientation of $\mathbf{m}_{\text{net}}$ of Mn_3Sn and $\mathbf{m}_{\text{FM}}$ of CoFeB, the produced out-of-plane polarized spin currents drive magnetization reversal in the respective layers. The intrinsically generated Oersted field, shifts the magnetic energy landscape of the Mn_3Sn, facilitating deterministic switching. The provided mechanisms explore a pathway to efficiently control magnetization and therefore spin-polarization.

References:

[1] T. Y. Lee, J. M. Lee, M. K. Kim, J. S. Oh, J. W. Lee, H. M. Jeong, P. H. Jang, M. K. Joo, K. Suh, S. H. Han, D.-E. Jeong, T. Kai, J. H. Jeong, J.-H. Park, J. H. Lee, Y. H. Park, E. B. Chang, Y. K. Park, H. J. Shin, Y. S. Ji, S. H. Hwang, K. T. Nam, B. S. Kwon, M. K. Cho, B. Y. Seo, Y. J. Song, G.

H. Koh, K. Lee, J.-H. Lee, G. T. Jeong, "World-Most Energy-Efficient MRAM Technology for Non-Volatile RAM Applications," in Proc. International Electron Devices Meeting (IEDM), San Francisco, CA, USA, 2022, pp. 10.7.1–10.7.4. https://doi.org/10.1109/IEDM45625.2022.10019430

[2] R. Saha, Y. P. Pundir, P. Kumar Pal, "Comparative Analysis of STT and SOT Based MRAMs for Last Level Caches," J. Magn. Magn. Mater., vol. 551, pp. 169161, 2022. https://doi.org/10.1016/j.jmmm.2022.169161

[3] F. Oboril, R. Bishnoi, M. Ebrahimi, M. B. Tahoori, "Evaluation of Hybrid Memory Technologies Using SOT-MRAM for On-Chip Cache Hierarchy," IEEE Trans. Comput.-Aided Design Integr. Circuits Syst., vol. 34, no. 3, pp. 367–380, 2015. https://doi.org/10.1109/TCAD.2015.2391254

[4] Q. Shao, P. Li, L. Liu, H. Yang, S. Fukami, A. Razavi, H. Wu, K. Wang, F. Freimuth, Y. Mokrousov, M. D. Stiles, S. Emori, A. Hoffmann, J. Åkerman, K. Roy, J.-P. Wang, S.-H. Yang, K. Garello, W. Zhang, "Roadmap of Spin–Orbit Torques," IEEE Trans. Magn., vol. 57, no. 7, pp. 1–39, 2021. https://doi.org/10.1109/TMAG.2021.3078583

[5] X. Qiu, Z. Shi, W. Fan, S. Zhou, H. Yang, "Characterization and Manipulation of Spin–Orbit Torque in Magnetic Heterostructures," Adv. Mater., vol. 30, no. 17, pp. 1705699, 2018. https://doi.org/10.1002/adma.201705699

[6] I. M. Miron, G. Gaudin, S. Auffret, B. Rodmacq, A. Schuhl, S. Pizzini, J. Vogel, P. Gambardella, "Current-Driven Spin Torque induced by the Rashba Effect in a Ferromagnetic Metal Layer," Nat. Mater., vol. 9, no. 3, pp. 230–234, 2010. https://doi.org/10.1038/nmat2613

[7] L. Liu, O. J. Lee, T. J. Gudmundsen, D. C. Ralph, R. A. Buhrman, "Current-Induced Switching of Perpendicularly Magnetized Magnetic Layers Using Spin Torque from the Spin Hall Effect," Phys. Rev. Lett., vol. 109, no. 9, pp. 096602, 2012. https://doi.org/10.1103/PhysRevLett.109.096602

[8] L. Liu, C.-F. Pai, Y. Li, H. W. Tseng, D. C. Ralph, R. A. Buhrman, "Spin-Torque Switching with the Giant Spin Hall Effect of Tantalum," Science, vol. 336, no. 6081, pp. 555–558, 2012. https://doi.org/10.1126/science.1218197

[9] I. M. Miron, K. Garello, G. Gaudin, P.-J. Zermatten, M. V. Costache, S. Auffret, S. Bandiera, B. Rodmacq, A. Schuhl, P. Gambardella, "Perpendicular Switching of a Single Ferromagnetic Layer induced by In-Plane Current Injection," Nature, vol. 476, pp. 189–193, 2011. https://doi.org/10.1038/nature10309

[10] K. Garello, F. Yasin, S. Couet, L. Souriau, J. Swerts, S. Rao, S. Van Beek, W. Kim, E. Liu, S. Kundu, D. Tsvetanova, K. Croes, N. Jossart, E. Grimaldi, M. Baumgartner, D. Crotti, A. Fumémont, P. Gambardella, G.S. Kar, "SOT-MRAM 300MM Integration for Low Power and Ultrafast Embedded Memories," in 2018 IEEE Symposium on VLSI Circuits, Honolulu, USA, pp. 81–82, 2018. https://doi.org/10.1109/VLSIC.2018.8502269

[11] V.D. Nguyen, S. Rao, K. Wostyn, S. Couet, "Recent Progress in Spin-Orbit Torque Magnetic Random-Access Memory," npj Spintronics, vol. 2, no. 1, pp. 48, 2024. https://doi.org/10.1038/s44306-024-00044-1

[12] S. Hu, D.-F. Shao, H. Yang, C. Pan, Z. Fu, M. Tang, Y. Yang, W. Fan, S. Zhou, E. Y. Tsymbal, X. Qiu, "Efficient Perpendicular Magnetization Switching by a Magnetic Spin Hall Effect in a Noncollinear Antiferromagnet," Nat. Comm., vol. 13, no. 1, pp. 4447, 2022. https://doi.org/10.1038/s41467-022-32179-2

[13] DC. Mahendra, D.-F. Shao, V. D.-H. Hou, A. Vailionis, P. Quarterman, A. Habiboglu, M. B. Venuti, F. Xue, Y.-L. Huang, C.-M. Lee, M. Miura, B. Kirby, C. Bi, X. Li, Y. Deng, S.-J. Lin, W. Tsai, S. Eley, W.-G. Wang, J. A. Borchers, E. Y. Tsymbal, S. X. Wang, "Observation of Anti-Damping Spin–Orbit Torques generated by In-Plane and Out-Of-Plane Spin Polarizations in MnPd3," Nat. Mater., vol. 22, no. 5, pp. 591–598, 2023. https://doi.org/10.1038/s41563-023-01522-3

[14] B. Pruckner, N. P. Jørstad, W. Goes, S. Selberherr, V. Sverdlov, "Field-Free Magnetization Switching in SOT-MRAM Devices with Noncollinear Antiferromagnets," Microelectron. Eng., vol. 300, pp. 112372, 2025. https://doi.org/10.1016/j.mee.2025.112372

[15] Z. He, L. Liu, "Magnetic Dynamics of Strained Non-Collinear Antiferromagnet," J. Appl. Phys., vol. 135, no. 9, pp. 093902, 2024. https://doi.org/10.1063/5.0192467

[16] T. Higo, K. Kondou, T. Nomoto, M. Shiga, S. Sakamoto, X. Chen, D. Nishio-Hamane, R. Arita, Y. Otani, S. Miwa, S. Nakatsuji, "Perpendicular Full Switching of Chiral Antiferromagnetic Order by Current," Nature, vol. 607, no. 7919, pp. 474–479, 2022. https://doi.org/10.1038/s41586-022-04864-1

[17] J.-Y. Yoon, P. Zhang, C.-T. Chou, Y. Takeuchi, T. Uchimura, J. T. Hou, J. Han, S. Kanai, H. Ohno, S. Fukami, L. Liu, "Handedness Anomaly in a Non-Collinear Antiferromagnet under Spin–Orbit Torque," Nat. Mater., vol. 22, no. 9, pp. 1106–1113, 2023. https://doi.org/10.1038/s41563-023-01620-2

[18] K. Nihei, T. Uchimura, J. Han, K. Gas, S. Kanai, H. Ohno, S. Fukami, "Temperature Dependence of Current-Induced Switching in Thin Epitaxial Films of Mn3Sn: Revealing the Dominant Role of Spin–Orbit Torque," Appl. Phys. Lett., vol. 127, no.13, pp. 132406, 2025. https://doi.org/10.1063/5.0294438

[19] T. Moriya, "Anisotropic Superexchange Interaction and Weak Ferromagnetism," Phys. Rev., vol. 120, no. 1, pp. 91–98, 1960. https://doi.org/10.1103/

PhysRev.120.91

[20] T. L. Gilbert, "A phenomenological theory of damping in ferromagnetic materials," IEEE Trans. Magn., vol. 40, no. 6, pp. 3443-3449,2004. https: //doi.org/10.1109/TMAG.2004.836740

[21] S. Fiorentini, M. Bendra, J. Ender, R. L. de Orio, W. Goes, S. Selberherr, V. Sverdlov, "Spin and Charge Drift-Diffusion in Ultra-Scaled MRAM Cells," Sci. Rep., vol. 12, no. 1,pp. 20958, 2022. https://doi.org/10.1038/s41598-022-25586-4

[22] J.-Y. Yoon, Y. Takeuchi, R. Takechi, J. Han, T. Uchimura, Y. Yamane, S. Kanai, J. Ieda, H. Ohno, S. Fukami, "Electrical Mutual Switching in a Noncollinear-Antiferromagnetic–Ferromagnetic Heterostructure," Nat. Comm., vol. 16, pp. 1171, 2025. https://doi.org/10.1038/s41467-025-56157-6

[23] P. M. Haney, H.-W. Lee, K.-J. Lee, A. Manchon, M. D. Stiles, "Current Induced Torques and Interfacial Spin-Orbit Coupling: Semiclassical Modeling," Phys. Rev. B, vol. 87, no. 17, pp. 174411, 2013. https://doi.org/10.1103/PhysRevB.87.174411

[24] L. Salemi, P. M. Oppeneer, "Theory of Magnetic Spin and Orbital Hall and Nernst Effects in Bulk Ferromagnets," Phys. Rev. B, vol. 106, no. 2, pp. 024410, 2022. https://doi.org/10.1103/PhysRevB.106.024410

[25] N. P. Jørstad, B. Pruckner, W. Goes, S. Selberherr, V. Sverdlov, "Spin Currents and Torques in Ferromagnetic Systems with Strong Interfacial Spin-Orbit Coupling," Scientific Reports, vol. 15, no. 1, pp. 38749, 2025. https://doi.org/10.1038/s41598-025-22567-1

[26] A. Brataas, Y. V. Nazarov, G. E. W. Bauer, "Finite-Element Theory of Transport in Ferromagnet–Normal Metal Systems," Phys. Rev. Lett., vol. 84, no. 11, pp. 2481–2484, 2000. https://doi.org/10.1103/PhysRevLett.84.2481

[27] V. P. Amin, M. D. Stiles, "Spin Transport at Interfaces with Spin-Orbit Coupling: Phenomenology," Phys. Rev. B, vol. 94, no. 10, pp. 104420, 2016. https://doi.org/10.1103/PhysRevB.94.104420

[28] S. Zhang, P. M. Levy, A. Fert, "Mechanisms of Spin-Polarized Current-Driven Magnetization Switching," Phys. Rev. Lett., vol. 88, no. 23, pp. 236601, 2002. https://doi.org/10.1103/PhysRevLett.88.236601

[29] X. Wang, A. Meng, Y. Yao, F. Lin, Y. Bai, X. Ning, B. Li, Y. Zhang, T. Nie, S. Shi, W. Zhao, "Large Field-Like Spin–Orbit Torque and Enhanced Magnetization Switching Efficiency Utilizing Amorphous Mo," Nano Lett., vol. 24, no. 23, pp. 6931-6938, 2024. https://doi.org/10.1021/acs.nanolett.4c01100

[30] S. X. Huang, T. Y. Chen, C. L. Chien, "Spin Polarization of Amorphous CoFeB Determined by Point-Contact Andreev Reflection," Appl. Phys. Lett., vol. 92, no. 24, pp. 242509, 2008. https://doi.org/10.1063/1.2949740

Contribution:
Bernhard Pruckner was responsible for conceptualization, formal analysis, methodology, software and writing of the original draft.
Nils Petter Jørstad was responsible for methodology, software and review and editing.
Wolfgang Goes was responsible for software.
Siegfried Selberherr was responsible for review and editing.
Viktor Sverdlov was responsible for supervision, project administration, resources and review and editing.

Acknowledgment and Sources of Funding:
The financial support by the Federal Ministry of Economy, Energy and Tourism, the National Foundation for Research, Technology and Development, and the Christian Doppler Research Association is gratefully acknowledged. The authors acknowledge TU Wien Bibliothek for financial support through its Open Access Funding Program.

Conflicts of Interest:
The authors have no conflicts of interest to declare that are relevant to the content of this article.